Optics & Laser Technology 144 (2021) 107391

Contents lists available at ScienceDirect

Optics and Laser Technology

journal homepage: www.elsevier.com/locate/optlastec

Effects of laser shock peening on the ultra-high cycle fatigue performance of additively manufactured Ti6Al4V alloy

Qinghong Jiang [a,b], Shuai Li [a,c], Cong Zhou [a], Bi Zhang [a,*], Yongkang Zhang [d]

[a] Department of Mechanical and Energy Engineering, Southern University of Science and Technology, Shenzhen 518055, China
[b] Department of Mechanical Engineering, Hong Kong Polytechnic University, Hong Kong Special Administrative Region
[c] School of Mechatronics Engineering, Harbin Institute of Technology, Harbin 150001, China
[d] School of Mechanical and Electrical Engineering, Guangdong University of Technology, Guangdong 510006, China

ARTICLE INFO

Keywords:
Metal additive manufacturing
Selective laser melting
Laser shock peening
Ultra-high cycle fatigue
Ti6Al4V titanium alloy

ABSTRACT

Although additive manufacturing (AM) allows to fabricate metallic parts with a high static strength comparable to their forged counterparts, the fatigue strength of an AM-ed part is generally inferior, restricting AM from many critical applications. In this study, laser shock peening (LSP) was applied to modify the surface properties of selective laser melting fabricated (SLM-ed) Ti6Al4V titanium alloy. This study performs systematic tests and analyses on the fabricated alloy specimens to characterize their microstructures and mechanical properties including residual stress, tensile strength, ultra-high cycle fatigue (UHCF) strength. The results reveal that LSP can refine microstructure, suppress residual stresses, and delay crack propagation in the affected area. However, the inherent defects in an SLM-ed part, such as unmelted powders, lack of fusion and clusters of α phase, dominate the fatigue failure of the specimens especially in the UHCF regime, resulting in their poor fatigue performance. Meanwhile, The LSP processed specimens showed a lower S-N curve than that of specimens without LSP processing especially in the UHCF regime, which not only results from the inherent defects, but also the increased surface roughness and non-uniform residual stresses.

1. Introduction

Titanium alloys have been widely applied to aerospace, automotive and biomedical industries due to their high specific strength, excellent corrosion resistance and ideal biocompatibility [1–3]. Traditionally, titanium alloy parts are manufactured from casting or forging blanks by the subtractive manufacturing (SM) techniques, including turning, milling, and grinding, etc. [4–6]. However, titanium alloys are known as typical difficult-to-machine materials with severe machining problems [7,8], including rapid tool wear, inferior surface quality, as well as very high buy-to-fly ratio (up to 40:1 for titanium in machining of an aerospace part) [9]. Such limitations dramatically increases the manufacturing cost of titanium alloy parts.

Selective laser melting is one of the most promising metal AM techniques due to its enormous advantages in rapid manufacturing [10], integrated manufacturing of complex parts [11], as well as lightweight design and manufacturing [12,13]. At present, it has been successfully applied to fabricate various metals [14–18].

However, the mechanical properties of an SLM part are significantly limited by the rough surface, high residual stress and internal defects. Generally, the surface roughness (Ra) of a part directly manufactured by SLM ranges from 10 μm to 20 μm [19]. Such poor surface roughness is mainly attributed to the inherent "stair-step" effect, balling phenomenon, partly melted powders adhered to surface, and inappropriate parameters [20–22]. Meanwhile, In an SLM process, the high energy density of a laser beam introduces a large temperature gradient when scanning at a high speed, which results in a non-uniform solidification, thus inducing tensile residual stresses (TRS) in the near-surface layers [22–24]. The TRS accumulates with an increase in part size, resulting in warpage, deformation, even interlaminar cracks in the final part [25,26]. Furthermore, the SLM process is prone to inducing internal defects [27]. Many previous studies have revealed that defects, such as pores, cracks, and lack of fusion, are easily induced during the complex SLM process [28,29]. When such parts are subjected to external loading, the defects serving as stress concentration sites may easily lead to crack initiation and propagation, ultimately reduce the fatigue life of the parts [30–32]. Besides, the anisotropic microstructures in an SLM-ed part are also a challenging issue [33,34].

* Corresponding author.
E-mail address: zhangb@sustech.edu.cn (B. Zhang).

https://doi.org/10.1016/j.optlastec.2021.107391
Received 27 November 2020; Received in revised form 2 July 2021; Accepted 9 July 2021
Available online 25 August 2021

Considerable efforts have been taken to address aforementioned problems in previous researches. Parameter optimization has been widely conducted to improve the quality of SLM-ed parts [35–37]. However, since an SLM process is influenced by numerous parameters [28,38], extensive studies are expected to be conducted to build a standard system for the SLM process [39]. On the other hand, the post-treatments such as surface machining (SM), heat-treatment (HT), hot isostatic pressing (HIP), mechanical shot peening (MSP), and laser shot peening (LSP) have been applied to further improve the mechanical properties of SLM-ed parts [40–43].

LSP is one of the most effective surface strengthening techniques to improve the mechanical properties of materials, including fatigue durability, wearability, and stress corrosion resistance [44–47]. During an LSP process, the beneficial compressive residual stress (CRS) and refined microstructure are introduced, which makes LSP a promising post-treatment process for SLM-ed parts [48,49]. Kalentics et al. [50] applied LSP to SLM-ed stainless steel, and demonstrated that LSP could effectively change the stress state from tensile to compressive. In a recent paper [51], Kalentics et al. proved that LSP is useful to reduce the crack density of the SLM-ed Ni-based superalloy. Sun et al. [52,53] compared the material properties of laser additive manufactured Ti6Al4V alloy before and after LSP, and found an effective improvement on elongation. However, systematic studies investigating the effect of LSP on the fatigue property of the SLM-ed titanium alloys are still absent.

As a promising manufacturing technique, the application of SLM is still restricted by the inferior fatigue performance of fabricated parts [59,60]. Fatigue data were collected from previous studies to analyze the fatigue performance of an SLM-ed Ti6Al4V alloy. All tensile specimens were horizontally built, which have higher fatigue strength with respect to their vertically build counterparts [61]. As shown in Fig. 1, the fatigue strength of SLM-ed Ti6Al4V specimens in the as-built condition is difficult to match that of casting specimens. It reaches the level of the casting after surface polishing. Additionally, the heat treatment could slightly improve the fatigue strength, but still can not be comparable to that of wrought counterparts.

Many studies related to the fatigue strength of SLM-ed parts have been carried out [30,54,62], mostly focusing on effects of the process parameters, defects in the parts, and post-treatment methods. Moreover, most of the fatigue experiments were conducted in low cycle ($N < 10^4$) or high cycle ($10^4 < N < 10^7$) fatigue regimes. However, with increasing needs in safety and reliability of a part, the fatigue life has been increased up to 10^9 cycles in critical applications, such as aerospace and marine engineering, high-speed rail system, wind power generation, and automotive manufacturing. Fortunately, the development of the ultrasonic fatigue test system makes it convenient to evaluate 10^9 to 10^{10} order fatigue strength by significantly increasing the loading frequency. For the first time, Wycisk et al. [57] analyzed the UHCF performance of SLM-ed Ti6Al4V, and demonstrated that fatigue strength was independent of the test frequency. Günther et al. [63] compared the UHCF strength of Ti6Al4V parts fabricated by SLM and EBM (Electron beam melting), and investigated the effects of defects in terms of their types, locations and sizes. Qian et al. [64] investigated the anisotropic UHCF behavior of SLM-ed Ti6Al4V, experimental results showed that fatigue strength decreased with the building orientation from 0°, 45°, to 90°. But systematic analyzes and experiments regarding the UHCF strength of SLM-ed alloy parts are still rarely reported.

For the first time, this work investigated the effects of LSP on the ultra-high cycle fatigue strength of SLM-ed Ti6Al4V. This study starts with the introduction of experimental preparation, followed by the characterization of microstructure, surface quality, and residual stress before and after LSP processing. Subsequently, the effects of LSP on tensile and UHCF strength are systematically compared to better understand the underlying impact mechanism. Finally, the comprehensive results and their relationship are discussed and revealed.

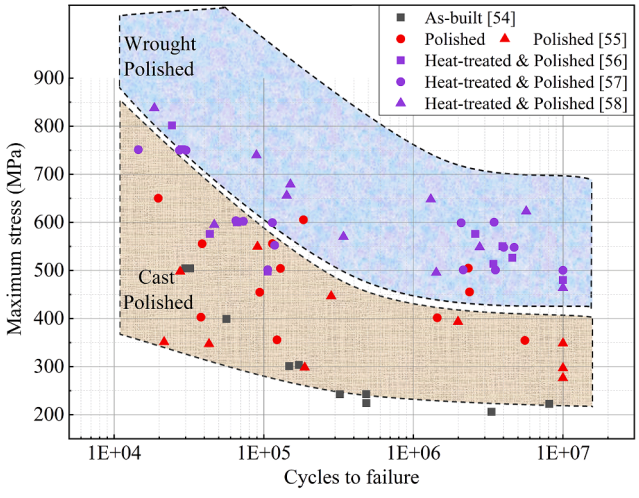

Fig. 1. Fatigue performance of SLM-ed Ti6Al4V specimens with different post treatments (R = 0.1, loading direction perpendicular to building direction) [54–58].

2. Experimental preparation

2.1. Material and SLM process

Ti6Al4V powders from Oerlikon were used to fabricate SLM specimens. Fig. 2**a** shows the SEM morphology and size distribution of applied powder with an average powder size of 16.72 μm. An SLM machine (Dimetal-100, Laseradd Tech of China) was adopted to

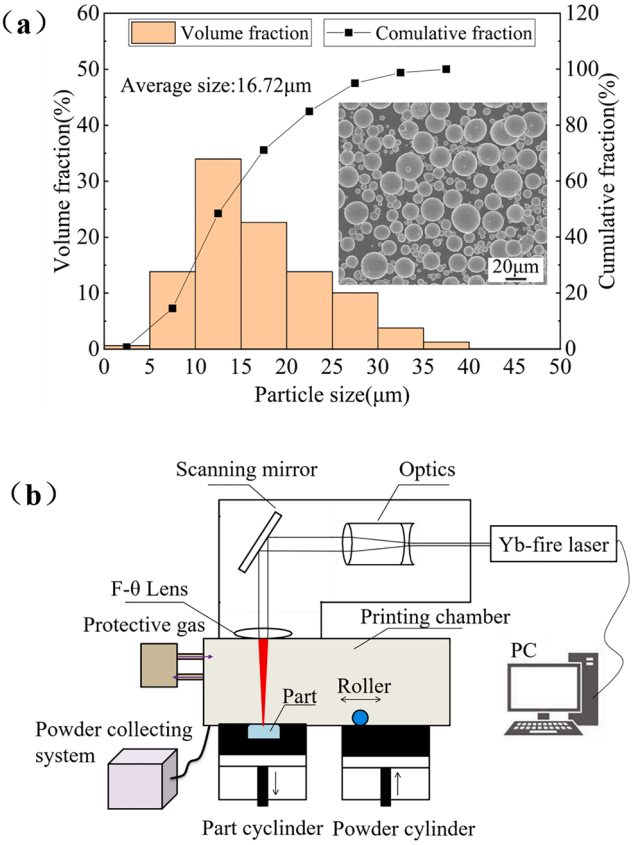

Fig. 2. (a) SEM image of Ti6Al4V powders and their size distribution, (b) Schematic arrangement of the SLM system.

fabricate Ti6Al4V specimens in the experiment. The SLM machine is schematically illustrated in Fig. 2**b**. The process parameters for SLM are displayed in Table 1. The zigzag scanning strategy in a layer was adopted with a rotated angle of 67° between successive layers [65].

2.2. Laser shock peening

As shown in Fig. 3, LSP utilizes a high energy density, short-duration pulsed laser to irradiate a sacrificial layer (black tape) through a constraint layer (water), the sacrificial layer absorbs the laser energy and forms rapidly expanding plasma, thereby generating a powerful shockwave that propagates into the workpiece. Plastic deformation is produced when the magnitude of shockwave exceeds the dynamic yield strength of the workpiece material. Meanwhile, high-density dislocation and CRS are induced to increase the material strength during the process [66,67].

In this study, plate samples with a size of 30 × 30 × 5 mm were fabricated by SLM for the material characterization and residual stress measurements before and after LSP processing, all samples were polished before testing. The LSP experiment was conducted in a PRO-CUDO® 200 laser peening system that was equipped with diode pumped pulsed YLF laser. The specimens were impacted by circular laser with a spot diameter of 3 mm and pulse width of 18 ns at an overlap of 50%. The heat treatment and LSP processing parameters are summarized in Table 2. In addition, the parameters of LSP2 was chosen to apply on tensile and UHCF test specimens, and all specimens were symmetrically impacted on both sides.

2.3. Material characterization

Surface topography and roughness were measured by VK-X100 Laser confocal microscope (SLAM). Residual stress was tested on an ESPI hole-drilling system (Prism Stresstech) according to the ASTM E837-08 standard. Drilling bits with a diameter 0.9 mm were applied in the test. The position of drilled hole for residual stress measurement is indicated in Fig. 4**a**, two positions were tested for each sample, and the average is taked in each depth. Fig. 4**b** shows the 3D morphology of drilled hole. Tensile and UHCF tests were conducted to evaluate the mechanical performance, the near-net-shape specimens were first additively manufactured, followed by surface grinding and polishing to obtain the final testing specimens.

Tensile test at room temperature was conducted on a universal testing machine (MTS Systems) at a tensile speed of 2 mm/min. An extensometer was applied to precisely measure Young's modulus (E) that is a critical parameter for specimen design in the ultra-high cycle fatigue test. Three tensile specimens were tested for each set, and a dimensional drawing of the tensile specimens is shown in Fig. 5**a** (The loading axis of tensile and fatigue specimens is perpendicular to the Z direction).

The UHCF test was carried out in a USF-2000 ultrasonic fatigue testing system, in which a loading frequency of 20 kHz could be achieved. The fatigue tests were performed under symmetrical tension–compression loading condition (R = 1). The schematic diagram of the ultra-high cycle fatigue specimen is shown in Fig. 5**b**. The final dimensions were determined as follows: $L_1 = 10$ mm, $b_1 = 1.5$ mm, $b_2 = 9$ mm, $W = 12$ mm, the resonance length L_2 was determined by the resonance condition. The amplitude of vibration displacement $u(x)$ deducing from the vibration equation is defined by Eq. (1) [68]:

Table 1
. Process parameters of SLM.

Laser power	Scanning speed	Layer thickness	Hatching spacing	Scanning strategy
190 W	1000 mm/s	0.03 mm	65 μm	67° rotation

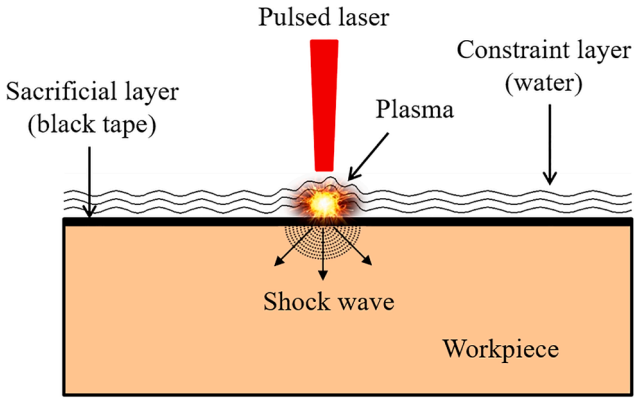

Fig. 3. Schematic diagram of LSP.

Table 2
. Processing conditions of the plate specimens.

Processing condition	AB	HT	LSP1	LSP2	LSP3
Heat treatment (°C)	—	955	955	955	955
LSP energy (J)/ Energy density (GW/cm^2)	—	—	5/ 3.93	7/ 5.50	9/ 7.08

Note: AB for machined as-built specimen; HT for heat-treated specimen at 955 °C in a vacuum for 2 h and then furnace cooling; LSP1, LSP2, and LSP3 for heat treated and processed by LSP at 5 J, 7 J, and 9 J, respectively.

$$\begin{aligned} U_x &= A_0\varphi(L_1,L_2)sinh(\beta x)exp(-\alpha x) \qquad |x| < L_1 \\ U_x &= A_0 cos[k(L-x)] \qquad\qquad\qquad L_1 < |x| < L \end{aligned} \tag{1}$$

where A_0 represents the vibration amplitude; $k = w/c$, $w = 2\pi f$, $c = (E/\rho)^{1/2}$; and α, β, φ are given by Eq. (2) [68]:

$$\begin{aligned} \alpha &= \frac{1}{2L_1}\ln\left(\frac{b_2}{b_1}\right) \\ \beta &= \sqrt{\alpha^2 - k^2} \\ \varphi(L_1,L_2) &= \frac{cos(kL_2)\exp(\alpha L_1)}{sinh(\beta L_1)} \end{aligned} \tag{2}$$

where f is loading frequency; E is Young's modulus; ρ is the density; and L_2 is obtained by combining and solving Eqs. Eqn 2.

$$L_2 = \frac{1}{k}arctan\left[\frac{1}{k}\left(\frac{\beta}{tanh(\beta L_1)} - \alpha\right)\right] \tag{3}$$

substituting the material parameters of HT into Eq. (3) gives $L_2 =$ 39.68 mm. Additionally, the maxmum applied stress can be calculated by Eq. (4):

$$\sigma_{max} = E\beta\varphi(L_1,L_2)A_0 \tag{4}$$

The applied stress is regulated by the vibration amplitude according to Eq. (4), the stable ultrasonic vibration accurately maintains applied stress during the test.

Machining accuracy and quality were strictly controlled to ensure that the fatigue specimens could produce resonance. The dimensional drawing of the fatigue specimens is shown in Fig. 5**c**. The schematic diagram of LSP on the fatigue specimens is presented in Fig. 5**d**.

3. Results

3.1. Microstructure

The microstructure of a material directly influences its mechanical properties. The representative 3D microstructure of a AB specimen is

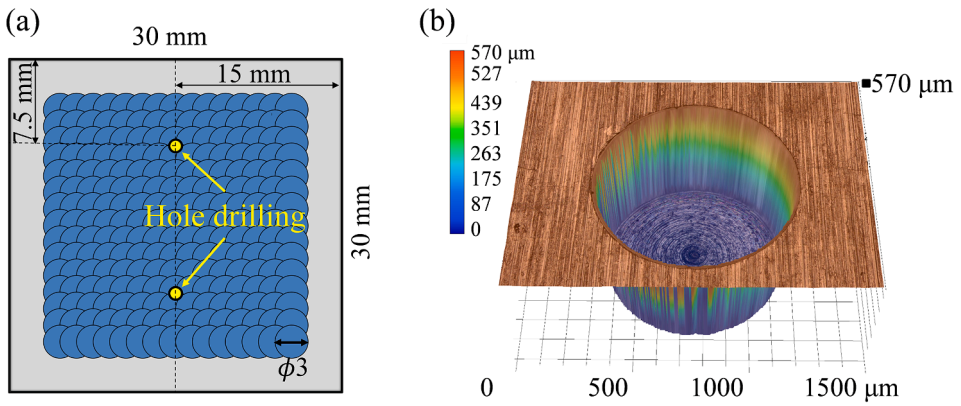

Fig. 4. (a) Schematic diagram of LSP processing and the position of drilled hole for residual stress measurement (Z represents the building direction in all figures), (b) 3D morphology of drilled hole.

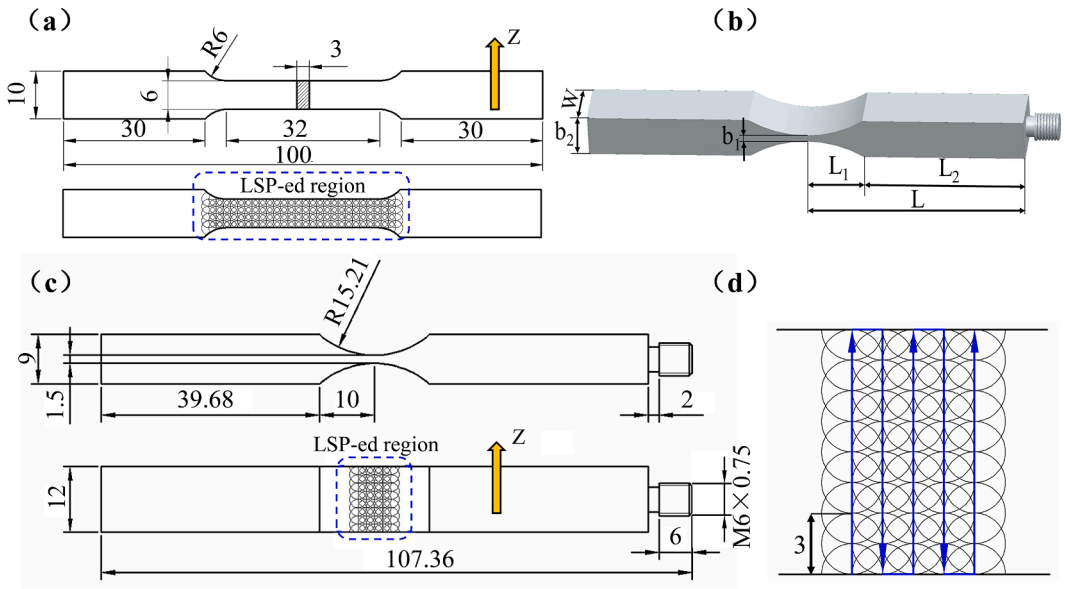

Fig. 5. (a) Dimensional drawing of tensile specimen, (b) Schematic diagram of the specimen for the ultra-high cycle fatigue test, (c) Dimensional drawing of the fatigue specimen, (d) Schematic diagram of LSP processing. (All dimensions are in mm).

shown in Fig. 6**a**. The microstructures of the Z-Y and Z-X views show typical prior β columnar grains running through multiple layers. The columnar grains were jagged and discontinuous due to the 67° rotation scanning strategy. In an SLM process, the previous layer is partially remelted under the heating of a laser beam, then acts as the nucleus to form the prior β columnar grain by epitaxial growth [69]. The microstructure within the columnar grains was full of the acicular α′ martensites (Fig. 6**c**), which was resulted from the large temperature gradient and high cooling rate [70,71]. The resultant α′ martensites are oriented at ±45° with respect to the building direction, because α′ martensite and prior β phase follow the burgers orientation relationship ($\{0\ 0\ 0\ 1\}_{\alpha'}//\{0\ 1\ 1\}_{\beta}$ and $[1210]_{\alpha'}//[1\ 1\ 1]_{\beta}$) during the rapid solidification process [72]. The X-Y view reveals equiaxed β grains, which is consistent with the hatching spacing in feature size. This morphology is the direct reflection of the scanning strategy of 67° rotation. A similar result was illustrated by Kumar et al. [65]. Heat treatment was conducted to homogenize the unfavorable as-built microstructure. Fig. 6**b** reveals the 3D micrograph of an HT specimen. The original acicular α′ martensites were transformed into the lamellar α + β microstructures (Fig. 6**d**), in which the lamellar α has an average size of 4.06 μm, and some prior β columnar grains still remain visible.

Fig. 7**a and b** exhibit the metallographic structures of HT parts before and after LSP2 processing. Before LSP processing, the grains in the near surface consisted of typical lamellar α + β phases with comparable feature size to grains in the substrate, the gain size of α phase (represented by the short axis) before LSP processing ranges from 3 to 6 μm. Fig. 7**c** illustrates the undeformed microstructures in the near surface. While gradient microstructures were induced in the near surface after LSP processing. As shown in Fig. 7**b**, severe plastic deformation (SPD) grains with grain size less than 2 μm can be observed in the top surface layer. Meanwhile, the grain size graded changing along the depth direction in LSP affected zone with the impact still visible up to 75 μm in depth. Fig. 7**d** illustrates the refined microstructures in the top surface layer.

3.2. Surface roughness and topography

Fig. 8 exhibits the surface roughness and topography of different sets of specimens. The HT specimens showed an average roughness Sa of 0.89 μm and a uniform surface topography although they carried visible grinding marks on their surfaces. The LSP process induced severe plastic deformation in the surface layer of specimens by the shockwave, which resulted in an increased surface roughness. For LSP1, LSP2, and LSP3, surface roughness Sa were increased to 2.08, 2.57, and 4.13 μm,

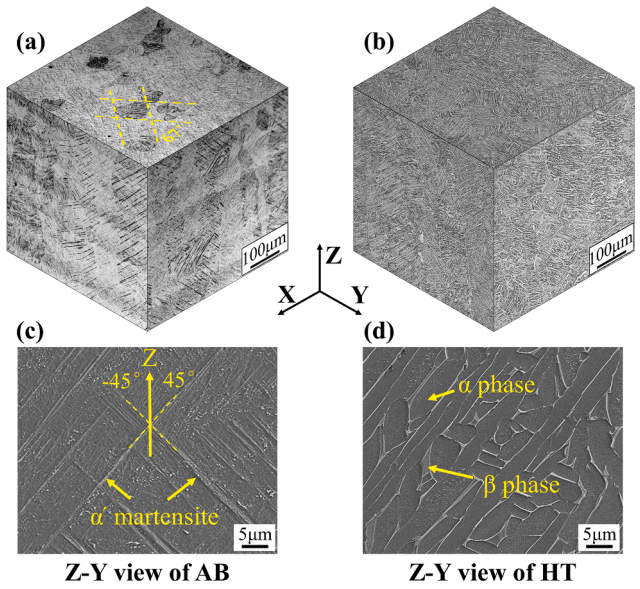

Fig. 6. Representative 3D microstructures: (a) AB specimen, (b) HT specimen, SEM images of Z-Y view (c) AB specimen, (d) HT specimen.

respectively. Meanwhile, the surface topography illustrated that plastic deformation became more distinct with an increase in laser energy, and the deformation in overlap regions was remarkable due to multiple impacts. Despite the increased surface roughness, the LSP process demonstrated more controllable surface damage by comparing with the traditional shot peening process, which is attributed to the non-mechanical interactions between laser beam and specimen, as well as the highly controllable energy levels [73–75].

3.3. Residual stress

The magnitude and distribution of residual stress have crucial influences on mechanical properties of a material, such as static strength, fatigue strength, creep and stress corrosion resistance [76,77]. For an SLM-ed part, the distribution of residual stress is determined by a complex thermal field which is further governed by material properties, part size, temperature distribution and process parameters [78].

The distribution of residual stresses (Maximum principal stress) in the surface layer of the flat samples is plotted in Fig. 9. The AB specimens revealed a very high TRS with an amplitude of 679 MPa at the depth of 40 μm, which is comparable to the results in published studies [79–81]. For the HT specimens, residual stress was significantly relieved, but the TRS with a amplitude of 104 MPa still existed in the near-surface. Compressive residual stress was obtained in the surface layer after LSP. For LSP1, LSP2, and LSP3, residual stresses with maximum CRS values of 86.9 MPa, 161.2 MPa and 214.1 MPa were induced in the depth of 80 μm, 106.8 μm and 121.6 μm, respectively. Additionally, the CRS in LSP2 and LSP3 were extended to the depth up to 500 μm.

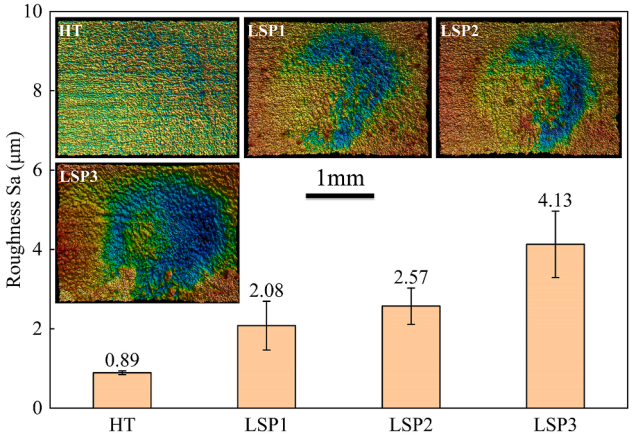

Fig. 8. Surface roughness and topography.

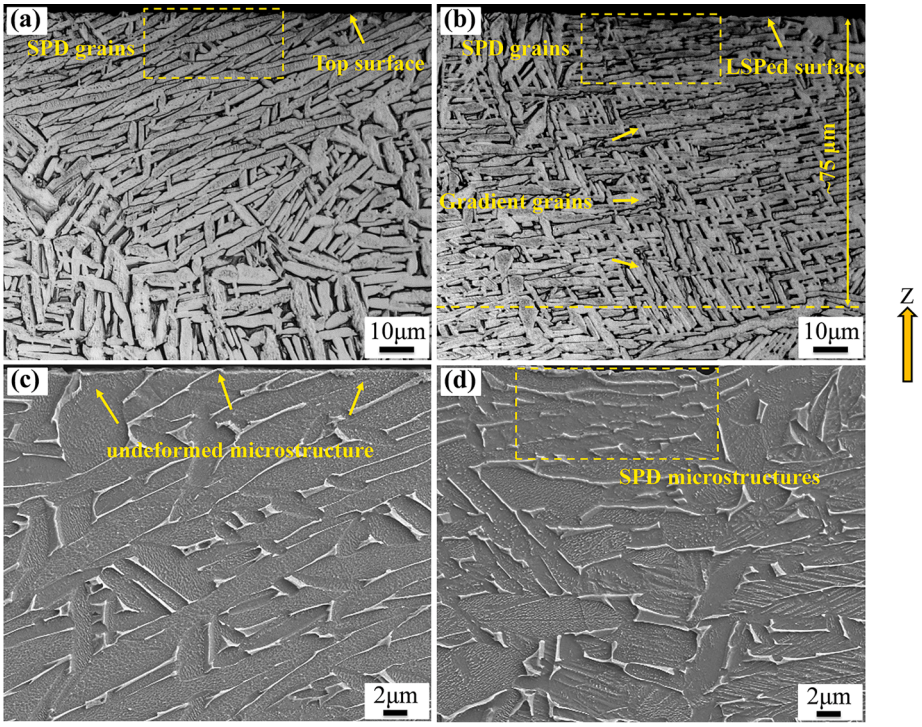

Fig. 7. Microstructures of HT parts in the near surface. Optical images: (a) before LSP, (b) After LSP (LSP2); SEM images: (a) before LSP, (b) After LSP (LSP2).

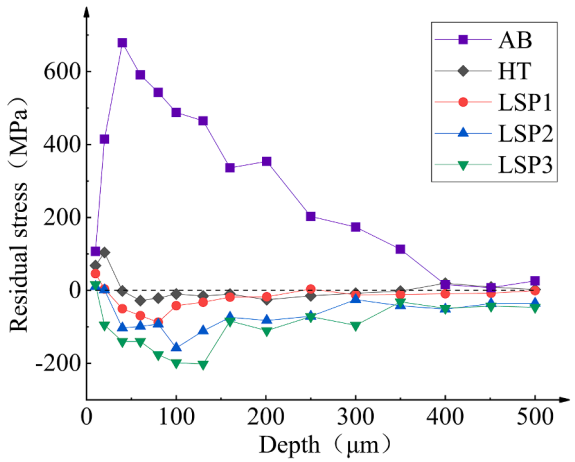

Fig. 9. Residual stress distributions in the surface layer of the flat samples.

3.4. Tensile strength

The stress–strain curves of different sets of specimens are shown in Fig. 10 with main results are summarized in Table 3. Consistent with previous studies [69,71,82], AB set exhibited a high ultimate tensile strength (1224 MPa) but a poor extensibility (3.32%), which is attributed to the acicular microstructures with a high resistance to deformation but a low deform capacity. After heat treatment, the tensile strength saw a significant decline, while the ductility showed a slight improvement. The LSP2 set shared a comparable tensile properties with HT set with exceptions of a lower elongation and Young's modulus.

Fracture analysis was conducted to better understand the underlying failure mechanism. The inherent defects in a AB specimen are marked with yellow arrows in Fig. 11**a**, the tearing ridges can be observed around such defects. These defects served as stress concentration sites, which accelerated the crack initiation and led to an early failure. The small dimples (2–3 μm) in Fig. 11**b** reflect plastic fracture in the AB specimen. Instead, Fig. 11**c** shows larger (2–5 μm) and deeper dimples in an HT specimen, which attributed to a better ductility. As shown in Fig. 11**d**, the edge of the HT fracture surface reveals a transcrystalline fracture with lamellar cleavage facets and a few dimples in between. After LSP processing, a similar transcrystalline fracture was shown in the edge of LSP2 fracture surface (Fig. 11**f**), but in which smoother cleavage facets was observed. Fig. 11**e** reveals a distinct tearing ridge paralleling to the surface, which demonstrates that crack propagated rapidly along the interface between the LSP affected area and the substrate during the failure process.

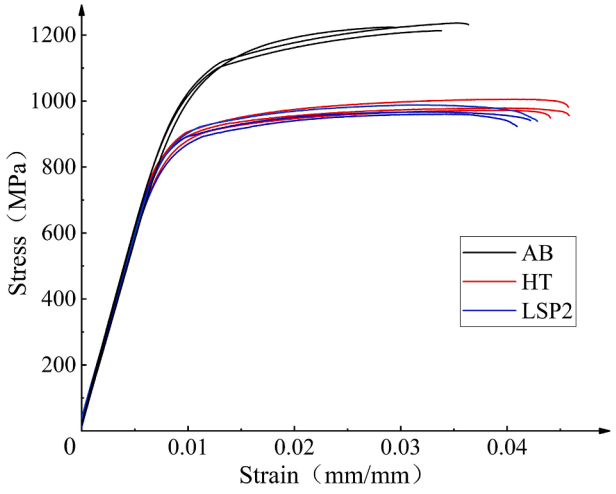

Fig. 10. Stress–strain curves of the test specimens.

Table 3
. Results of the tensile tests.

Condition	UTS (MPa)	Elongation (%)	*E* (GPa)
AB	1224.9 ± 11.6	3.32 ± 0.35	116.9 ± 4.8
HT	974.2 ± 33.2	4.53 ± 0.08	119.1 ± 3.3
LSP2	969.6 ± 9.8	4.12 ± 0.09	116.4 ± 4.5

3.5. Fatigue strength

Fig. 12 compares S-N curves before and after LSP2, the test was set at 1×10^9 cycles. Both curves show a continuing decline rather than a traditional fatigue limit in the UHCF regime, which is consistent with the results in previous studies [57,63]. The LSP set exhibits a comparable fatigue strength to HT set in the high cycle fatigue regime. However, larger disparity of fatigue strength between both sets occurred with the increasing of loading cycle in the UHCF regime, especially the fatigue limit was 270 MPa in the HT specimens and 210 MPa in the LSP2 specimens at 10^9 cycles.

Fig. 13a presents the macroscopic fracture surfaces of HT specimens in which the fatigue fracture areas were marked with yellow dashed lines. Multiple crack initiation sites were observed when a higher stress was applied (3 crack initiation sites: $\sigma = 400$ MPa; 2 crack initiation sites: $\sigma = 340$ MPa), but only one crack initiation site was identified when loading was in the ultra-high cycle fatigue regime (1 crack initiation site: $\sigma = 280$ MPa). Most fatigue failures in HT specimens were triggered by the defects located in the near-surface, including unmelted powders (Fig. 13**b**), lack of fusion (Fig. 13**c**) and clusters of α phase (Fig. 13**d**). These defects result in stress concentration and inferior bonding strength, which facilitates crack initiation, expansion, and finally premature failure. Conversely, the specimen showed a higher fatigue strength when there are no apparent defects in the fracture surface (Fig. 13**e**). For instance, an HT specimen survived until 3.57×10^7 cycles under a maximum stress $\sigma = 370$ MPa. The fatigue life was one order of magnitude higher than that of the specimens under the equivalent loading.

The original defects in the SLM-ed specimens dominated the fatigue failure with most fatigue failures were initiated from the defects in the near surface. However, different crack-initiation modes were observed in LSP2 fatigue fracture surfaces, cracks tend to initiate from the middle portion of the side surface or internal defects. Fig. 14**a** presents the macroscopic view of the fatigue fracture surface of an LSP2 specimen failed at 1.38×10^5 cycles under $\sigma = 340$ MPa. The main crack initiated from the middle portion of the side surface which was not subjected to the LSP2 processing. Fig. 14**c** shows the crack initiation site, while the small fatigue striations are revealed in Fig. 14**d**. As indicated by the dotted arrows in Fig. 14**a**, most cracks propagated outwards from the initiation site, but the cracks extending to the surface changed their propagation direction and propagated along the direction parallel to the surface in the LSP affected area (as indicated by the solid arrows). The enlarged view in Fig. 14**b** shows that the local cracks deviated from the direction parallel to the surface and expanded to the inside, which demonstrated the hindering effect to crack propagation in the LSP affected area. As shown in Fig. 14**e**, the crack originated from an internal defect in an LSP2 specimen failed at 7.72×10^7 cycles under $\sigma = 230$ MPa. These observations in the LSP fatigue fracture surfaces suggest the strengthening effect of LSP.

However, the fatigue failure was triggered by a surface micro notch in an LSP2 specimen failed at 4.35×10^8 cycles under $\sigma = 220$ MPa (Fig. 14**f**). The LSP2 specimens showed a lower S-N curve than that of the HT specimens especially in the UHCF regime, which not only results from the inherent defects, but also the increased surface roughness and non-uniform residual stresses. The positive and negative effects of the LSP processing have a competitive relationship, the details are discussed

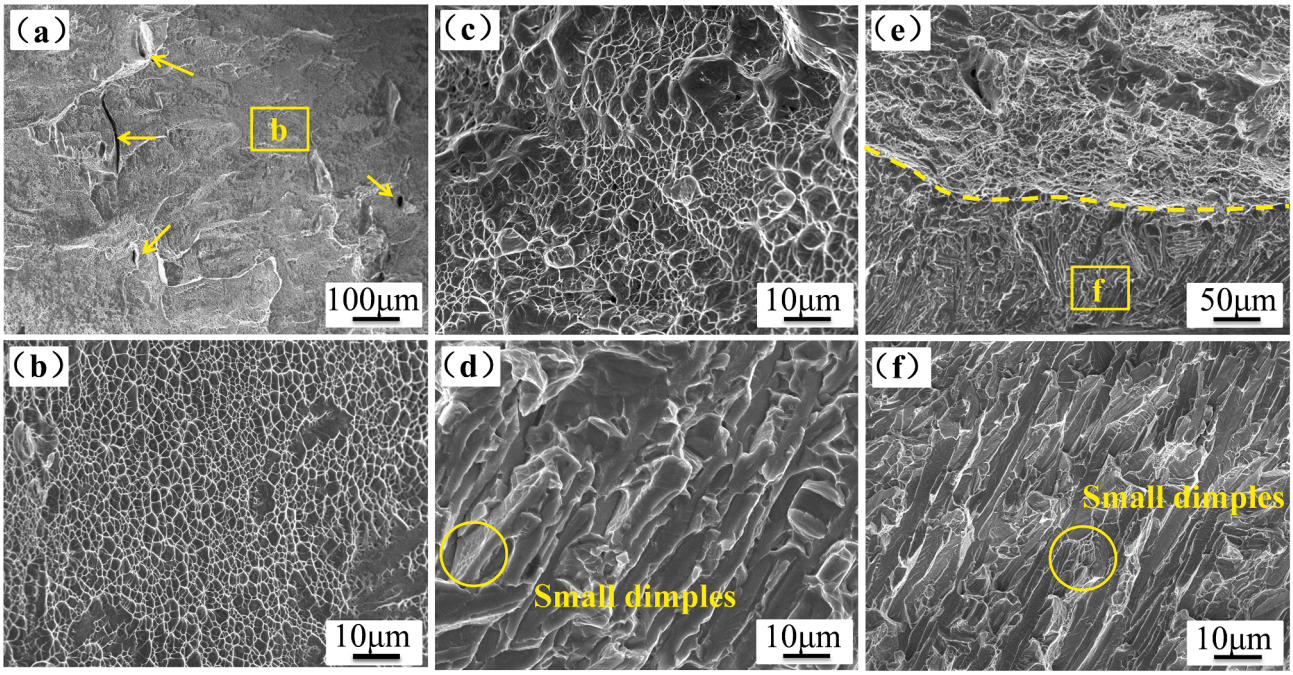

Fig. 11. SEM fracture morphologies: (a) AB, (b) Enlarged view of boxed b in Fig. 11a, (c)(d) HT, (e) LSP2, (f) Enlarged view of boxed f in Fig. 11e.

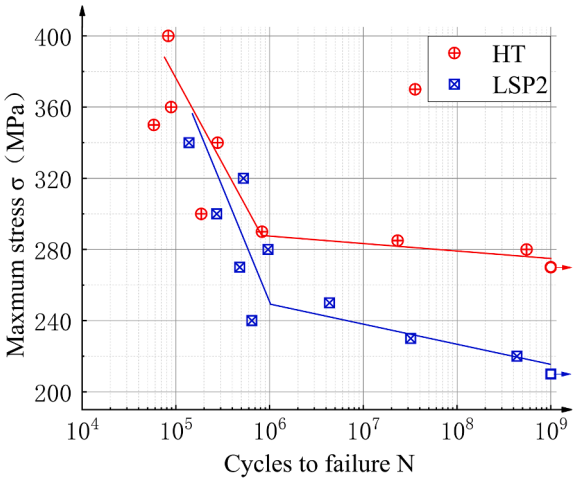

Fig. 12. S-N curves before and after LSP.

in the next section.

4. Discussion

The comprehensive results presented above show the effects of LSP on surface properties of the SLM-ed Ti6Al4V specimens, including microstructure, surface roughness and residual stress, as well as the mechanical properties such as tensile and urtra-high fatigue strengths. On this basis, their underlying interactions are discussed in details below.

In an LSP process, the pulsed laser induces shock waves with high pressure (GPa level), which results in plastic strain with gradient distribution in the material surface [83]. The influence of LSP extends to the depth where the shock wave pressure exceeds the material Hugoniot elastic limit (*HEL*) which is given by Eq. (5) [84],

$$HEL = \frac{1-v}{1-2v}\sigma_{dyn} \tag{5}$$

where v is the Poisson's ratio, σ_{dyn} is the dynamic yield strength of the material.

As revealed in the 3.1 section, the refined grains were induced in the LSP influenced area. According to previous studies [52,66,85], dislocation movement and deformation twins are the two mechanisms to induce refined grains in the Ti6Al4V specimens during an LSP process. Theoretically, the strength of a material can be improved by reducing the grain size according to the Hall-Petch relationship [86]. With grain refinement, more grains in the influenced area are turned to have different orientations and more grain boundaries are induced, which inhibits the dislocations from crossing, traveling and accumulating between grains, thereby delaying the crack propagation and improving the material strength. This phenomenon works up to a specific grain size below which the strength starts to drop with further reduction in grain size [87,88].

The inherent TRS in an SLM-ed part is known to deteriorate mechanical properties of the part. As shown in Fig. 9, the high TRS existed in the surface of the as-built specimen, which was effectively relieved by the subsequent heat treatment. Further, LSP translated the residual stress in the surface from tensile to compressive state. The induced CRS reduces the effective applied stress and stress intensity factors at the crack tip, and simultaneously causes a crack closure effect, which decreases the crack propagation rate [51].

Refined grains and CRS are the two primary mechanisms that LSP can improve the material properties [49,50]. As observed in Fig. 14**a**, the fatigue cracks in an LSP specimen were turned to propagate along the direction parallel to the surface, which reveals the retardation effect of LSP on fatigue crack propagation. A similar phenomenon was observed in the tensile fracture surface.

Although LSP processing induced beneficial microstructure and CRS, the fatigue properties were affected more by the inherent defects, which greatly overshadowed the positive effects of LSP. As analyzed in the 3.5 section, the inherent defects promoted the crack nucleation and early propagation which account for the most of the fatigue life in an UHCF test [89]. Consequently, most fatigue crack initiated from the inherent defects including unmelted powders, lack of fusion and clusters of α phase, the defect-dominated fatigue behavior was also clarified in the previous study [90].

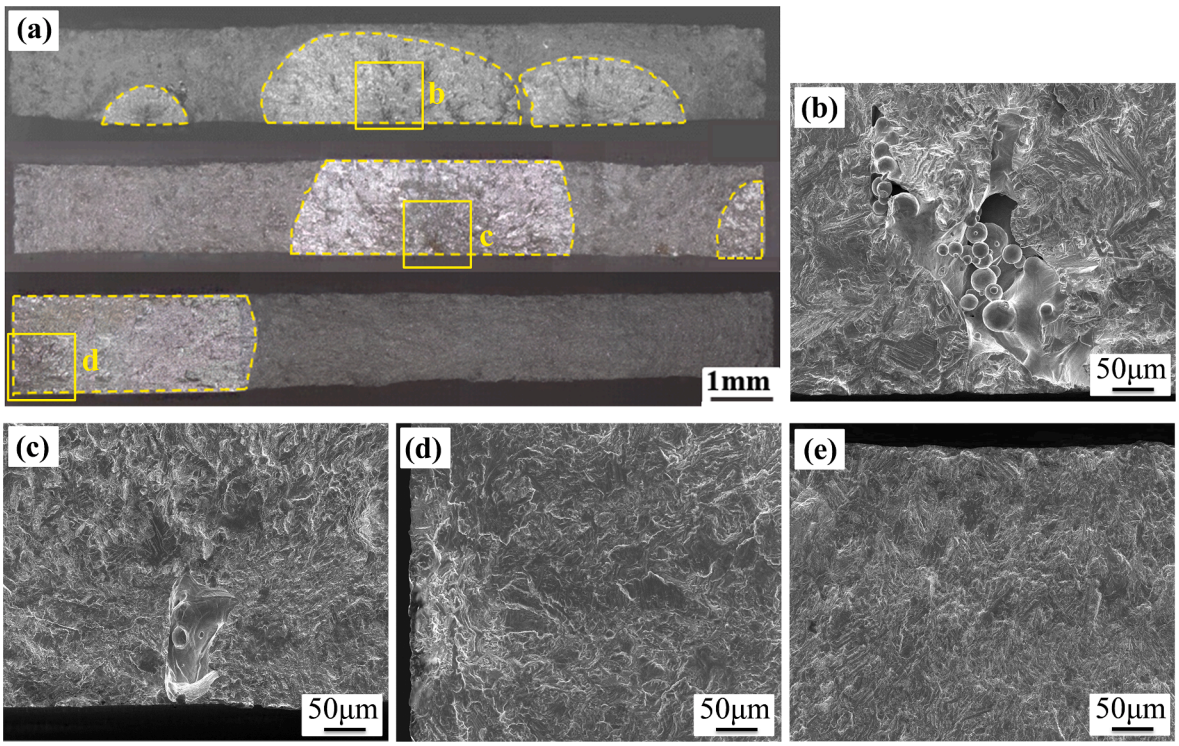

Fig. 13. (a) Macroscopic views of the fracture surfaces of the HT specimens, Enlarged views of b, c, d in (a) are shown (b)(c) and (d), respectively. (b) Unmelted powders ($\sigma = 400$ MPa, $N = 8.29 \times 10^4$ cycles), (c) Lack of fusion ($\sigma = 340$ MPa, $N = 2.78 \times 10^5$ cycles), (d) Clusters of α phase ($\sigma = 280$ MPa, $N = 5.52 \times 10^8$ cycles), (e) $\sigma = 370$ MPa, $N = 3.57 \times 10^7$ cycles.

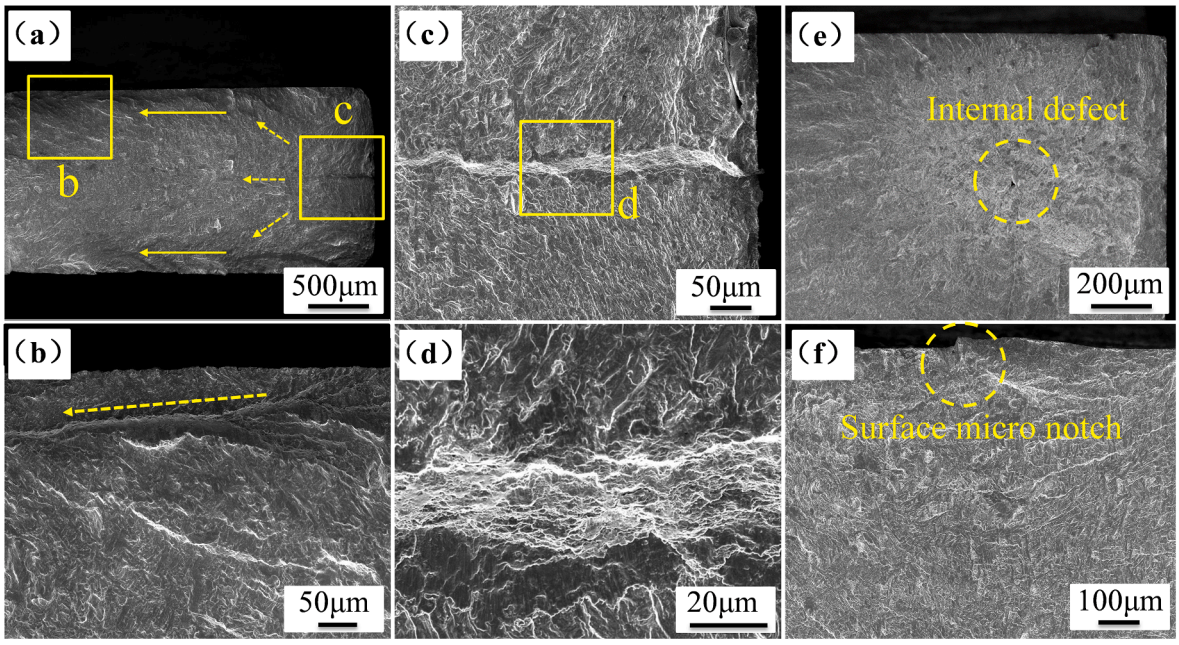

Fig. 14. SEM images of LSP fatigue fracture surface: (a) $\sigma = 340$ MPa, $N = 1.38 \times 10^5$ cycles, (b) Enlarged view of b in (a), (c) Enlarged view of c in (a), (d) Enlarged view of d in (c), (e) $\sigma = 230$ MPa, $N = 7.72 \times 10^7$ cycles, (f)$\sigma = 220$ MPa, $N = 4.35 \times 10^8$ cycles.

On the other hand, the surface roughness increased to 2.57 μm (Sa) after LSP2 processing, the rougher surface induces surface damage (micro notches) on the surface, which has significant adverse impacts on the final fatigue strength especially in the UHCF regime, consequently, leads to a decline S-N curve after LSP processing. Meanwhile, the UHCF performance is influenced by the distribution of residual stress. Fig. 15 presents the schematic illustrations of residual stress distribution in UHCF specimen after LSP processing. According to the principle of equilibrium, the symmetric LSP processing induces CRS in both sides, but a tensile stress core in the midsection of the specimens [91]. This leads to a higher crack growth rate and explains why fatigue crack was initiated from an internal defect in Fig. 14**e**. Moreover, the resultant CRS in the cambered surface was non-uniform in both X and Z directions, which may lead to a decline in mechanical strength [92]. Especially, the

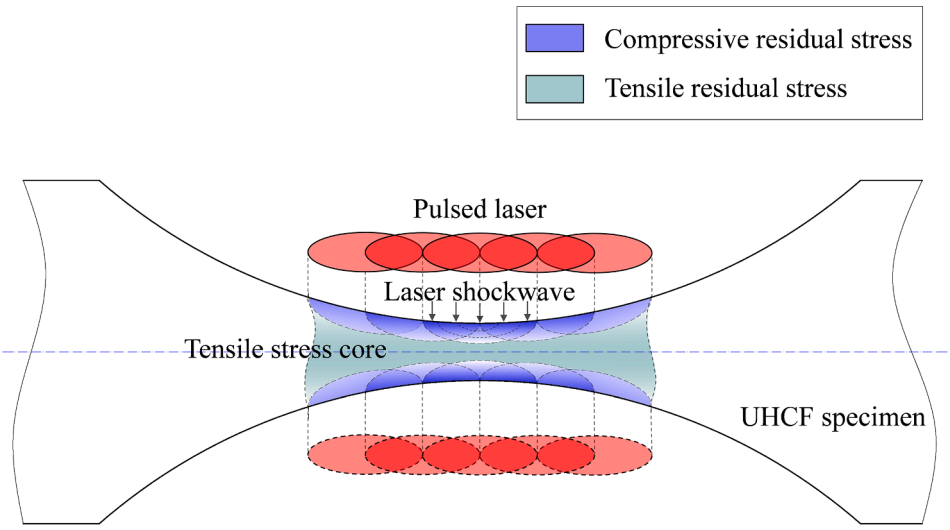

Fig. 15. Schematic illustrations of residual stress distribution in UHCF specimen after LSP processing.

fatigue specimens applied in this study with the variable cross-sections have a higher stress magnification coefficient M in the fracture section ($M = 5.2$), given by Eq. (6), which significantly increases the stress sensitivity of fatigue failure.

$$M = \frac{\beta \times \varphi}{k} \tag{6}$$

where β, φ, k are given in the 2.3 section.

On this basis, although the LSP processing reinforced the surface layers of SLM-ed parts by changing their microstructure and residual stress, the final static strength did not show obvious improvement. Moreover, the result of fatigue test shows an inverse effect after LSP especially in the UHCF regime due to inherent defects, increased surface roughness and non-uniform residual stresses. Therefore, in order to maximize the potential of the combination between SLM and LSP, the defects in SLM-ed parts must be controlled. Meanwhile, the schemes to associate two advanced techniques need further explorations.

5. Conclusions

In this study, the effects of the LSP processing on properties of the SLM-ed Ti6Al4V specimens were systematically studied. The main findings are drawn as follows:

(1) In the SLM process, high cooling rate and temperature gradient resulted in high TRS and anisotropic microstructure in the as-built Ti6Al4V specimens. With the heat treatment at 955 °C, the residual stress was significantly relieved, and the original acicular α′ martensite was transformed into the lamellar α + β microstructures.
(2) The S-N curves continued to decline in the UHCF regime before and after LSP. Most HT fatigue failures were triggered by inherent defects, including unmelted powders, lack of fusion and existence of the clusters of the α phase. Additionally, the number of crack initiation sites decreased with a decrease in applied stress.
(3) LSP processing was able to refine the microstructure and induce CRS in the near-surface layers of SLM-ed specimens, and the strengthening effect of LSP was identified in the local fracture surface. However, the fatigue strength of the specimens showed a degradation after the LSP processing, which was caused by inherent defects, as well as increased surface roughness and non-uniform residual stresses.

SLM has a great potential in the fabrication of metallic parts, however, the post-treatments, such as heat treatment, surface machining, and LSP processing, are necessary to improve the mechanical properties of an SLM-ed part. This study illustrated that inherent defects play a major role in the UHCF performance of SLM-ed Ti6Al4V parts. And LSP processing has the potential to serve as an ideal strengthening treatment if the original defects, surface damage, and stress distribution are well controlled.

CRediT authorship contribution statement

Qinghong Jiang: Investigation, Methodology, Conceptualization, Writing – original draft, Writing - review & editing. **Shuai Li:** Formal analysis, Writing - review & editing. **Cong Zhou:** Writing - review & editing. **Bi Zhang:** Conceptualization, Supervision, Writing - review & editing. **Yongkang Zhang:** Resources.

Declaration of Competing Interest

The authors declare that they have no known competing financial interests or personal relationships that could have appeared to influence the work reported in this paper.

Acknowledgements

This work was supported by the International Cooperation Research Plan of Shenzhen (Grant No. GJHZ20180411143506667), and the National Natural Science Foundation of China (Grant No. 51775117).

References

[1] C. Leyens, M. Peters, Titanium and titanium alloys: fundamentals and applications, 2003.
[2] H.X. Jin, K.X. Wei, J.M. Li, J.Y. Zhou, W. Peng, Research development of titanium alloy in aerospace industry, Chin. J. Nonferr. Met. 25 (2) (2015) 280–292.
[3] L.C. Zhang, L.Y. Chen, A review on biomedical titanium alloys: recent progress and prospect, Adv. Eng. Mater. 21 (4) (2019) 1–29.
[4] A. Aramcharoen, Influence of cryogenic cooling on tool wear and chip formation in turning of titanium alloy. 7th HPC 2016 - CIRP Conference on High Performance Cutting, 2016.
[5] A. Shokrani, V. Dhokia, S.T. Newman, Investigation of the effects of cryogenic machining on surface integrity in CNC end milling of Ti-6Al-4V titanium alloy, J. Manuf. Processes 21 (2016) 172–179.
[6] L.D. Zhu, Z.C. Yang, Z.B. Li, Investigation of mechanics and machinability of titanium alloy thin-walled parts by CBN grinding head, Int. J. Adv. Manuf. Technol. 100 (9–12) (2019) 2537–2555.
[7] D. Ulutan, T. Ozel, Machining induced surface integrity in titanium and nickel alloys: A review, Int. J. Mach. Tools Manuf 51 (3) (2011) 250–280.

[8] X.L. Liang, Z.Q. Liu, B. Wang, State-of-the-art of surface integrity induced by tool wear effects in machining process of titanium and nickel alloys: A review, Measurement 132 (2019) 150–181.
[9] B. Dutta, F.H. Froes, The additive manufacturing of titanium alloys, Adv. Mater. Res. 1019 (2014) 19–25.
[10] K. Vaideeswaran, O. Sereda, Y. Zangui, H. Saudan, M. Dadras, Effect of processing parameters on microstructure and mechanical properties of additively manufactured stainless steel, Eur. Microsc. Congr. 2016: Proc. (2016).
[11] D. Wang, Y.M. Wang, S.B. Wu, H. Lin, Y.Q. Yang, S.C. Fan, C. Gu, J.H. Wang, C. H. Song, Customized a Ti6Al4V Bone Plate for Complex Pelvic Fracture by Selective Laser Melting, Materials 10 (1) (2017) 1–14.
[12] D. Walton, H. Moztarzadeh, Design and development of an additive manufactured component by topology optimisation, Procedia CIRP 60 (2017) 205–210.
[13] Z. Li, D.Z. Zhang, P. Dong, I. Kucukkoc, A lightweight and support-free design method for selective laser melting, Int. J. Adv. Manuf. Technol. 90 (9–12) (2016) 2943–2953.
[14] C.F. Tey, X.P. Tan, S.L. Sing, W.Y. Yeong, Additive manufacturing of multiple materials by selective laser melting: Ti-alloy to stainless steel via a Cu-alloy interlayer, Addit. Manuf. 31 (2020), 100970.
[15] M. Pröbstle, S. Neumeier, J. Hopfenmüller, L.P. Freund, T. Niendorf, D. Schwarze, M. Göken, Superior creep strength of a nickel-based superalloy produced by selective laser melting, Mater. Sci. Eng., A 674 (2016) 299–307.
[16] A. Kreitcberg, V. Brailovski, S. Turenne, Effect of heat treatment and hot isostatic pressing on the microstructure and mechanical properties of Inconel 625 alloy processed by laser powder bed fusion, Mater. Sci. Eng., A 689 (2017) 1–10.
[17] Y. Zhou, S.F. Wen, B. Song, X. Zhou, Q. Teng, Q.S. Wei, Y.S. Shi, A novel titanium alloy manufactured by selective laser melting: Microstructure, high temperature oxidation resistance, Mater. Des. 89 (2016) 1199–1204.
[18] L.C. Zhang, H. Attar, Selective laser melting of titanium alloys and titanium matrix composites for biomedical applications: a review, Adv. Eng. Mater. 18 (4) (2016) 463–475.
[19] Z. Chen, X. Wu, D. Tomus, C.H.J. Davies, Surface roughness in Selective Laser Melted Ti-6Al-4V alloy components, Addit. Manuf. 21 (2018) 91–103.
[20] G. Strano, L. Hao, R.M. Everson, K.E. Evans, Surface roughness analysis, modelling and prediction in selective laser melting, J. Mater. Process. Technol. 213 (4) (2013) 589–597.
[21] F. Calignano, Investigation of the accuracy and roughness in the laser powder bed fusion process, Virtual Phys. Prototyping 13 (1) (2018) 1–8.
[22] Y. Liu, Y. Yang, D. Wang, A study on the residual stress during selective laser melting (SLM) of metallic powder, Int. J. Adv. Manuf. Technol. 87 (1–4) (2016) 1–10.
[23] L. Van Belle, G. Vansteenkiste, J.C. Boyer, Investigation of residual stresses induced during the selective laser melting process, Key Eng. Mater. 554–557 (2013) 1828–1834.
[24] Z.C. Fang, Z.L. Wu, C.G. Huang, C.W. Wu, Review on residual stress in selective laser melting additive manufacturing of alloy parts, Opt. Laser Technol. 129 (2020), 106283.
[25] I. Yadroitsev, I. Yadroitsava, Evaluation of residual stress in stainless steel 316L and Ti6Al4V samples produced by selective laser melting, Virtual Phys. Prototyping 10 (2) (2015) 67–76.
[26] L. Thijs, F. Verhaeghe, T. Craeghs, J.V. Humbeeck, J.-P. Kruth, A study of the microstructural evolution during selective laser melting of Ti–6Al–4V, Acta Mater. 58 (9) (2010) 3303–3312.
[27] S. Cao, Z. Chen, C.V.S. Lim, K. Yang, Q. Jia, T. Jarvis, D. Tomus, X. Wu, Defect, microstructure, and mechanical property of Ti-6Al-4V alloy fabricated by high-power selective laser melting, JOM 69 (12) (2017) 2684–2692.
[28] B. Zhang, Y.T. Li, Q. Bai, Defect formation mechanisms in selective laser melting: a review, Chin. J. Mech. Eng. 30 (3) (2017) 515–527.
[29] H. Gong, K. Rafi, H. Gu, T. Starr, B. Stucker, Analysis of defect generation in Ti–6Al–4V parts made using powder bed fusion additive manufacturing processes, Addit. Manuf. 1–4 (2014) 87–98.
[30] P. Edwards, M. Ramulu, Fatigue performance evaluation of selective laser melted Ti–6Al–4V, Mater. Sci. Eng., A 598 (2) (2014) 327–337.
[31] Q.C. Liu, J. Elambasseril, S.J. Sun, M. Leary, M. Brandt, P.K. Sharp, The Effect of Manufacturing Defects on the Fatigue Behaviour of Ti-6Al-4V Specimens Fabricated Using Selective Laser Melting, Adv. Mater. Res. 891–892 (2014) 1519–1524.
[32] J.W. Pegues, M.D. Roach, N. Shamsaei, Additive manufacturing of fatigue resistant austenitic stainless steels by understanding process-structure-property relationships, Mater. Res. Lett. 8 (1) (2020) 8–15.
[33] R. Rashid, S.H. Masood, D. Ruan, S. Palanisamy, R.R.A. Rahman, J. Elambasseril, M. Brandt, Effect of energy per layer on the anisotropy of selective laser melted AlSi12 aluminium alloy, Addit. Manuf. 22 (2018) 426–439.
[34] K. Kunze, T. Etter, J. Grässlin, V. Shklover, Texture, anisotropy in microstructure and mechanical properties of IN738LC alloy processed by selective laser melting (SLM), Mater. Sci. Eng. A 620 (2015) 213–222.
[35] B. Song, S. Dong, H. Liao, C. Coddet, Process parameter selection for selective laser melting of Ti6Al4V based on temperature distribution simulation and experimental sintering, Int. J. Adv. Manuf. Technol. 61 (9–12) (2012) 967–974.
[36] K. Kempen, L. Thijs, J.V. Humbeeck, J.P. Kruth, Processing AlSi10Mg by selective laser melting: Parameter optimisation and material characterisation, Mater. Sci. Technol. 31 (8) (2015) 917–923.
[37] M. Krishnan, E. Atzeni, R. Canali, F. Calignano, D. Manfredi, E.P. Ambrosio, L. Iuliano, On the effect of process parameters on properties of AlSi10Mg parts produced by DMLS, Rapid Prototyping J. 20 (6) (2014) 449–458.
[38] N.T. Aboulkhair, N.M. Everitt, I. Ashcroft, C. Tuck, Reducing porosity in AlSi10Mg parts processed by selective laser melting, Addit. Manuf. 1–4 (2014) 77–86.
[39] J. Sun, Y. Yang, D. Wang, Parametric optimization of selective laser melting for forming Ti6Al4V samples by Taguchi method, Opt. Laser Technol. 49 (2013) 118–124.
[40] W. Tillmann, C. Schaak, J. Nellesen, M. Schaper, M.E. Aydinöz, K.P. Hoyer, Hot isostatic pressing of IN718 components manufactured by selective laser melting, Addit. Manuf. 13 (2017) 93–102.
[41] G.M. Ter Haar, T.H. Becker, Selective Laser Melting Produced Ti-6Al-4V: Post-Process Heat Treatments to Achieve Superior Tensile Properties, Materials 11 (1) (2018) 1–15.
[42] S. Milton, A. Morandeau, F. Chalon, R. Leroy, Influence of Finish Machining on the Surface Integrity of Ti6Al4V Produced by Selective Laser Melting, Procedia CIRP 45 (2016) 127–130.
[43] N.E. Uzan, S. Ramati, R. Shneck, N. Frage, Yeheskel, On the effect of shot-peening on fatigue resistance of AlSi10Mg specimens fabricated by additive manufacturing using selective laser melting (AM-SLM), Addit. Manuf. 21 (2018) 458–464.
[44] J.Z. Lu, K.Y. Luo, Y.K. Zhang, C.Y. Cui, G.F. Sun, J.Z. Zhou, L. Zhang, J. You, K. M. Chen, J.W. Zhong, Grain refinement of LY2 aluminum alloy induced by ultra-high plastic strain during multiple laser shock processing impacts, Acta Mater. 58 (11) (2010) 3984–3994.
[45] A. King, A. Steuwer, C. Woodward, P.J. Withers, Effects of fatigue and fretting on residual stresses introduced by laser shock peening, Mater. Sci. Eng., A 435–436 (2006) 12–18.
[46] Y.Q. Li, X.D. Wang, Z.F. Yang, F.L. Song, Wear resistance of copper improved by laser shock peening, High Power Laser Particle Beams 28 (2) (2016) 1–5.
[47] Y. Liao, C. Ye, G.J. Cheng, A review: warm laser shock peening and related laser processing technique, Opt. Laser Technol. 78 (2016) 15–24.
[48] N. Kalentics, E. Boillat, P. Peyre, C. Gorny, C. Kenel, C. Leinenbach, J. Jhabvala, R. E. Logé, 3D Laser Shock Peening-A new method for the 3D control of residual stresses in Selective Laser Melting, Mater. Des. 130 (2017) 350–356.
[49] N. Kalentics, K. Huang, M.O.V. de Seijas, A. Burn, V. Romano, R.E. Loge, Laser shock peening: A promising tool for tailoring metallic microstructures in selective laser melting, J. Mater. Process. Technol. 266 (2019) 612–618.
[50] N. Kalentics, E. Boillat, P. Peyre, S. Ćirić-Kostić, N. Bogojević, R.E. Logé, Tailoring residual stress profile of Selective Laser Melted parts by Laser Shock Peening, Addit. Manuf. 16 (2017) 90–97.
[51] N. Kalentics, N. Sohrabi, H.G. Tabasi, S. Griffiths, J. Jhabvala, C. Leinenbach, A. Burn, R.E. Logé, Healing cracks in selective laser melting by 3D laser shock peening, Addit. Manuf. 30 (2019), 100881.
[52] G. Wei, R. Sun, B. Song, Z. Ying, L. Fei, Z. Che, L. Bo, G. Chao, L. Lei, P. Peng, Laser shock peening of laser additive manufactured Ti6Al4V titanium alloy, Surf. Coat. Technol. 349 (2018) 503–510.
[53] R. Sun, L. Li, Y. Zhu, W. Guo, P. Peng, B. Cong, J. Sun, Z. Che, B. Li, C. Guo, L. Liu, Microstructure, residual stress and tensile properties control of wire-arc additive manufactured 2319 aluminum alloy with laser shock peening, J. Alloy. Compd. 747 (2018) 255–265.
[54] E. Wycisk, C. Emmelmann, S. Siddique, F. Walther, High Cycle Fatigue (HCF) Performance of Ti-6Al-4V Alloy Processed by Selective Laser Melting, Adv. Mater. Res. 816–817 (2013) 134–139.
[55] H. Gong, K. Rafi, H. Gu, G.D. Janaki Ram, T. Starr, B. Stucker, Influence of defects on mechanical properties of Ti–6Al–4V components produced by selective laser melting and electron beam melting, Mater. Des. 86 (2020) 545–554.
[56] E. Wycisk, A. Solbach, S. Siddique, D. Herzog, F. Walther, C. Emmelmann, Effects of Defects in Laser Additive Manufactured Ti-6Al-4V on Fatigue Properties, Phys. Procedia, 56, 371–378.
[57] E. Wycisk, S. Siddique, D. Herzog, F. Walther, C. Emmelmann, Fatigue Performance of Laser Additive Manufactured Ti–6Al–4V in Very High Cycle Fatigue Regime up to 10^9 Cycles, Front. Mater. 2 (72) (2015) 1–8.
[58] F. Palm, Fatigue performance of additive manufactured TiAl6V4 using electron and laser beam melting, Int. J. Fatigue 94 (2017) 211–217.
[59] K. Wegener, A.B. Spierings, T.L. Starr, Fatigue performance of additive manufactured metallic parts, Rapid Prototyping J. 19 (2) (2013) 88–94.
[60] M. Waddell, K. Walker, R. Bandyopadhyay, K. Kapoor, A. Mallory, X. Xiao, A. C. Chuang, Q. Liu, N. Phan, M.D. Sangid, Small fatigue crack growth behavior of Ti-6Al-4V produced via selective laser melting: In situ characterization of a 3D crack tip interactions with defects, Int. J. Fatigue 137 (2020), 105638.
[61] R. Molaei, A. Fatemi, N. Sanaei, J. Pegues, N. Shamsaei, S. Shao, P. Li, D.H. Warner, N. Phan, Fatigue of additive manufactured Ti-6Al-4V, Part II: The relationship between microstructure, material cyclic properties, and component performance, Int. J. Fatigue 132 (2020), 105363.
[62] M. Benedetti, V. Fontanari, M. Bandini, F. Zanini, S. Carmignato, Low- and high-cycle fatigue resistance of Ti-6Al-4V ELI additively manufactured via selective laser melting: Mean stress and defect sensitivity, Int. J. Fatigue 107 (2018) 96–109.
[63] J. Günther, D. Krewerth, T. Lippmann, S. Leuders, T. Tröster, A. Weidner, H. Biermann, T. Niendorf, Fatigue life of additively manufactured Ti–6Al–4V in the very high cycle fatigue regime, Int. J. Fatigue 94 (2017) 236–245.
[64] G.A. Qian, Y.F. Li, D.S. Paolino, A. Tridello, F. Berto, Y. Hong, Very-high-cycle fatigue behavior of Ti-6Al-4V manufactured by selective laser melting: Effect of build orientation, Int. J. Fatigue 136 (2020), 105628.
[65] P. Kumar, O. Prakash, U. Ramamurty, Micro-and meso-structures and their influence on mechanical properties of selectively laser melted Ti-6Al-4V, Acta Mater. 154 (2018) 246–260.
[66] X.D. Ren, W.F. Zhou, F.F. Liu, Y.P. Ren, S.Q. Yuan, N.F. Ren, S.D. Xu, T. Yang, Microstructure evolution and grain refinement of Ti-6Al-4V alloy by laser shock processing, Appl. Surf. Sci. 363 (2016) 44–49.

[67] Y. Yang, H. Zhang, H. Qiao, Microstructure characteristics and formation mechanism of TC17 titanium alloy induced by laser shock processing, J. Alloy. Compd. 722 (2017) 509–516.
[68] H.Q. Xue, H. Tao, C. Bathias, The design of specimen for fatigue test at ultrasonic frequency, Acta Aeronautica Et Astronautica Sinica 25 (4) (2004) 425–428.
[69] T. Vilaro, C. Colin, J.D. Bartout, As-Fabricated and Heat-Treated Microstructures of the Ti-6Al-4V Alloy Processed by Selective Laser Melting, Metall. Mater. Trans. A 42 (10) (2011) 3190–3199.
[70] X.L. Zhao, S.J. Li, M. Zhang, Y.D. Liu, T.B. Sercombe, S.G. Wang, Y.L. Hao, R. Yang, L. Murr, Comparison of the microstructures and mechanical properties of Ti–6Al–4V fabricated by selective laser melting and electron beam melting, Mater. Des. 95 (2016) 21–31.
[71] H.K. Rafi, N.V. Karthik, H. Gong, T.L. Starr, B.E. Stucker, Microstructures and Mechanical Properties of Ti6Al4V Parts Fabricated by Selective Laser Melting and Electron Beam Melting, J. Mater. Eng. Performance 22 (12) (2013) 3872–3883.
[72] A.A. Antonysamy, J. Meyer, P.B. Prangnell, Effect of build geometry on the β-grain structure and texture in additive manufacture of Ti6Al4V by selective electron beam melting, Mater. Charact. 84 (2013) 153–168.
[73] A.K. Gujba, M. Medraj, Laser Peening Process and Its Impact on Materials Properties in Comparison with Shot Peening and Ultrasonic Impact Peening, Materials 7 (12) (2014) 7925–7974.
[74] Y.K. Gao, Improvement of fatigue property in 7050–T7451 aluminum alloy by laser peening and shot peening, Mater. Sci. Eng. A 528 (10) (2011) 3823–3828.
[75] K.K. Liu, M.R. Hill, The effects of laser peening and shot peening on fretting fatigue in Ti–6Al–4V coupons, Tribol. Int. 42 (9) (2009) 1250–1262.
[76] S. Prabhakaran, A. Kulkarni, G. Vasanth, S. Kalainathan, P. Shukla, V. K. Vasudevan, Laser shock peening without coating induced residual stress distribution, wettability characteristics and enhanced pitting corrosion resistance of austenitic stainless steel, Appl. Surf. Sci. 428 (2018) 17–30.
[77] J.H. Moon, S.M. Baek, S.G. Lee, Y. Seong, A. Amanov, S. Lee, H.S. Kim, Effects of residual stress on the mechanical properties of copper processed using ultrasonic-nanocrystalline surface modification, Mater. Res. Lett. 7 (3) (2019) 97–102.
[78] P. Mercelis, Residual stresses in selective laser sintering and selective laser melting, Rapid Prototyping J. 12 (5) (2006) 254–265.
[79] Z. Xiao, C. Chen, H. Zhu, Z. Hu, B. Nagarajan, L. Guo, X. Zeng, Study of residual stress in selective laser melting of Ti6Al4V, Mater. Des. 193 (2020), 108846.
[80] T. Mishurova, S. Cabeza, K. Artzt, J. Haubrich, M. Klaus, C. Genzel, G. Requena, G. Bruno, An assessment of subsurface residual stress analysis in SLM Ti-6Al-4V, Materials 10 (4) (2017) 348.
[81] J.L. Bartlett, X. Li, An overview of residual stresses in metal powder bed fusion, Addit. Manuf. 27 (2019) 131–149.
[82] B. Vandenbroucke, J.P. Kruth, Selective laser melting of biocompatible metals for rapid manufacturing of medical parts, Rapid Prototyping J. 13 (4) (2007) 196–203.
[83] C.S. Montross, T. Wei, L. Ye, G. Clark, Y.W. Mai, Laser Shock Processing and its Effects on Microstructure and Properties of Metal Alloys: A Review, Int. J. Fatigue 24 (10) (2002) 1021–1036.
[84] J.N. Johnson, R.W. Rohde, Dynamic Deformation Twinning in Shock-Loaded Iron, J. Appl. Phys. 42 (11) (1971) 4171.
[85] S.J. Lainé, K.M. Knowles, P.J. Doorbar, R.D. Cutts, D. Rugg, Microstructural characterisation of metallic shot peened and laser shock peened Ti–6Al–4V, Acta Mater. 123 (2017) 350–361.
[86] N. Hansen, Hall-Petch relation and boundary strengthening, Scr. Mater. 51 (8) (2004) 801–806.
[87] M. Gol'dshtein, B. Bronfin, A. Shifman, V. Osipov, Mechanism of grain boundary strengthening of steels, Met. Sci. Heat Treat. 21 (2) (1979) 104–109.
[88] H. He, Y. Yi, S. Huang, Y. Zhang, An improved process for grain refinement of large 2219 Al alloy rings and its influence on mechanical properties, J. Mater. Sci. Technol. 35 (1) (2019) 55–63.
[89] Y. Hong, A. Zhao, G. Qian, Essential characteristics and influential factors for Very-High-Cycle fatigue behavior of metallic materials, Acta Metallurgica Sinica -Chinese Edition 45 (7) (2009) 769–780.
[90] A. Masayuki, U. Yoshihiko, K. Toshifumi, N. Masaki, K. Ryosei, Defect-dominated fatigue behavior in type 630 stainless steel fabricated by selective laser melting, Mater. Sci. Eng. A 66 (2016) 19–26.
[91] A. Chahardehi, F.P. Brennan, A. Steuwer, The effect of residual stresses arising from laser shock peening on fatigue crack growth, Eng. Fract. Mech. 77 (11) (2010) 2033–2039.
[92] K.Y. Luo, B. Liu, L.J. Wu, Z. Yan, J.Z. Lu, Tensile properties, residual stress distribution and grain arrangement as a function of sheet thickness of Mg–Al–Mn alloy subjected to two-sided and simultaneous LSP impacts, Appl. Surf. Sci. 369 (2016) 366–376.